Title

Graph-based rotational nonuniformity correction for localized compliance measurement in the human nasopharynx.

Journal

Biomedical Optics Express, 12(4)

ISSN

2156-7085

Authors

Miao, Yusi
Jing, Joseph J
Chen, Zhongping

Publication Date

2021-04-01

DOI

10.1364/boe.419997

Peer reviewed

Research Article | Vol. 12, No. 4 / 1 April 2021 / Biomedical Optics Express 2508
Biomedical Optics EXPRESS

Graph-based rotational nonuniformity correction for localized compliance measurement in the human nasopharynx

YUSI MIAO,[1,2] JOSEPH J. JING,[1] AND ZHONGPING CHEN[1,2,3,*]

[1]Beckman Laser Institute, University of California, Irvine, Irvine, CA 92612, USA
[2]Department of Biomedical Engineering, University of California, Irvine, Irvine, CA 92697, USA
[3]The Edwards Lifesciences Center for Advanced Cardiovascular Technology, University of California, Irvine, Irvine, CA 92697, USA
*z2chen@uci.edu

Abstract: Recent advancements in the high-speed long-range optical coherence tomography (OCT) endoscopy allow characterization of tissue compliance in the upper airway, an indicator of collapsibility. However, the resolution and accuracy of localized tissue compliance measurement are currently limited by the lack of a reliable nonuniform rotational distortion (NURD) correction method. In this study, we developed a robust 2-step NURD correction algorithm that can be applied to the dynamic OCT images obtained during the compliance measurement. We demonstrated the utility of the NURD correction algorithm by characterizing the local compliance of nasopharynx from an awake human subject for the first time.

1. Introduction

Measurement of tissue mechanical properties can provide important information about the presence and status of disease [1–3]. In airway, underlying elastic properties of tissue are typically measured as compliance, which can affect the flow behavior and indicates the region with high collapsibility [4–6]. In addition, airway compliance is considered as one of the metrics to identify and evaluate the treatment effectiveness of patients with obstructive sleep apnea (OSA) [7,8] or obstructive pulmonary disorders [9,10]. The measurement of airway compliance typically involves generating continuous intraluminal positive or negative pressure while the dynamic changes in the cross-sectional area or volume in the airway are captured by a real-time imaging device over a course of time of a respiratory cycle. However, the accuracy of the airway compliance measurement is highly dependent on the imaging techniques as the tissue displacement is typically subtle. Elastography in the respiratory tract and lungs has been previously quantified using ultrasound (US) [11,12] and magnetic resonance imaging (MRI) [13,14]. However, few approaches have the capability to achieve adequate spatial and temporal resolution for compliance testing of the upper airway. In addition, MRI is costly, and may not be suitable for routine clinical examination.

Recently, long-range optical coherence tomography (OCT) has been introduced to provide minimally invasive and high-resolution anatomical scanning of the airway [15–18]. Since OCT is a non-contact fiber optic-based imaging technique, a flexible endoscopic can be used in combination with the clinical videoscope in awake or sedated patients. In addition, a long-range OCT system has an exceptionally long imaging distance of typically >10 mm to capture the entire lumen in adult upper airway [15,17,19]. Previously, airway compliance measurement has been obtained using endoscopic OCT and can be divided into cross-sectional compliance (CC) [20,21] and localized compliance (LC) measurement [6,22]. CC of the airway is obtained by segmenting the cross-sectional area of the lumen at the same anatomical location and dividing the changes in the luminal area over changes in pressure. On the other hand, regional tissue

#419997 https://doi.org/10.1364/BOE.419997
Journal © 2021 Received 21 Jan 2021; revised 8 Mar 2021; accepted 11 Mar 2021; published 30 Mar 2021

Biomedical Optics EXPRESS

elasticity of the airway can be obtained as LC by dividing the lumen into smaller segments and assessing the contribution of each part. Both methods assume the axial deformation of the upper airway is negligible compared to the radial expansion in the lumen.

Although the LC measurement can reveal regional elasticity differences of airway tissue and provide a detailed spatial mapping of compliance, motion artifacts and nonuniform rotation distortion (NURD) can significantly affect the accuracy of compliance measurement. While motion artifacts from heart-beat and breathing can be avoided by simply increasing the imaging speed, such as implementing a high-speed micromotor, NURD correction is typically more challenging and has to be corrected by an image registration algorithm once the images are acquired [23–25]. In addition, most of the existing algorithms are designed to correct NURD in static images rather than dynamic images, where there may be a motion in a specific part of the image, which can add additional challenges to the correction algorithm. Further discussions on the previous NURD correction methods are included in the section 3.

In this study, we developed a robust 2-step NURD correction method based on the intensity signal from the micromotor wire and the imaging sheath. To demonstrate the feasibility of the method, we captured the dynamic deformation in the upper airway in an awake adult volunteer during a respiratory cycle. Once the NURD correction algorithm was applied, an automated-edge detection algorithm based on graph cuts was applied to the lumen to measure the LC. To the best of our knowledge, this is the first demonstration of LC measurement in an awake human subject using OCT imaging.

2. Methods

2.1. High-speed micromotor imaging system

The long-range OCT imaging system and micromotor imaging probe used in this study have been previously described [17]. Briefly, the imaging system employs a 100 kHz vertical cavity surface emitting laser (VCSEL, Thorlabs Inc., NJ) with a center wavelength of 1300 nm and a bandwidth of 100 nm. A high-speed balanced detector (PDB480C-AC, Thorlabs Inc., NJ) and a high-speed data acquisition card (ATS9373, AlazarTech, QC, Canada) are utilized to achieve high sampling density of the interference signal for an extended imaging range. Due to the narrow instantaneous linewidth of the VCSEL source, the coherence length is longer than 1 m and the sensitivity roll-off in the signal is predominantly due to the limited bandwidth of the acquisition devices. In this study, we achieved an imaging range of 25 mm using the k-clock signal generated from a 48 mm external Mach-Zehnder interferometer. The imaging probe consisted of a commercial 0.9 mm micromotor (Kinetron, Netherlands), a micromirror, and a focusing optic element which were placed into an 8 mm long, 1.2 mm diameter glass capillary. A 45-degree mirror with a 0.9 mm outer diameter was positioned onto the shaft of the motor to reflect the light in the orthogonal direction with respect to the catheter. The imaging probe was further protected by a 1.8 mm diameter transparent sheath. During a respiratory cycle, OCT imaging was performed at 200 frame-per-seconds (500 A-scan/frame) to capture the dynamic movement of the nasopharynx. The axial resolution of the system was measured to be 8 μm and the lateral resolution at the focal point of the probe was 110 μm. The relatively low lateral resolution is due to the extended working distance (20 mm) of the imaging probe.

2.2. Dynamic airway imaging of a human patient

Before OCT imaging, the upper airway of the patient was locally anesthetized and decongested with a 4% lidocaine/oxymetazonline HCl nasal spray. After 5 minutes when the nasal cavity was reported to be numb, the imaging probe was inserted into the nose and guided through the nasopharynx using patient feedback as well as OCT imaging (**Fig. 1**). During the dynamic compliance measurement, the patient was asked to inhale and exhale air at approximately 60

Biomedical Optics EXPRESS

breaths-per-minute. In addition to OCT, pressure measurement was simultaneously performed at the nasal cavity using a commercial 3.5F pressure catheter (Mikro-Cath, Millar, BA) to monitor the changes in intraluminal pressure. The patient reported minimal discomfort during the measurement.

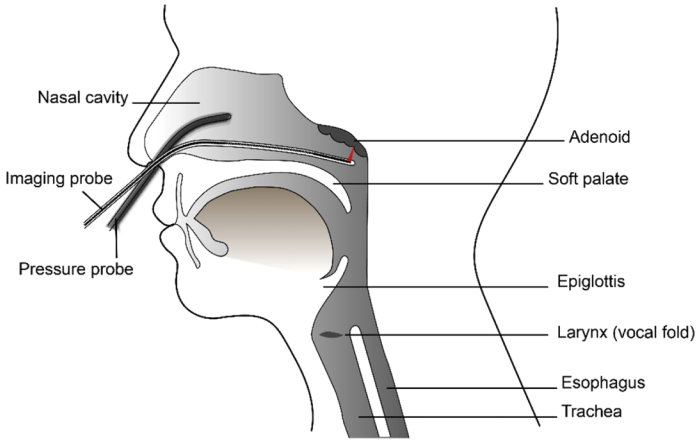

Fig. 1. A schematic diagram showing the sagittal plane of airway anatomical structure and the placement of the imaging probe. The pressure probe was inserted and guided to nasal cavity through a separate nostril from the imaging probe.

2.3. NURD correction algorithm

In our study, a cross-section of the lumen is acquired as a series of polar OCT images with 1000 × 1000 pixels. In the polar coordinate, the horizontal axis indicates the angle of the probe rotation and the vertical axis indicates depth. **Figure 2** shows the center portion of OCT images that contains the catheter sheath displayed in polar and Cartesian coordinates. Before applying the NURD correction algorithm, we manually selected the region that contains glass capillary, sheath, and wire indicated in Fig. 2, and cropped out the rest of the OCT signals. This pre-processing step is necessary to remove certain imaging artifacts and the back reflection from the tissue that may interfere with our NURD correction algorithm.

The proposed NURD correction algorithm is a 2-step process that uses the structural landmarks from the wire and the surface profile of the catheter sheath to correct local distortion. During the first step of the NURD correction, the location of the metal wire is identified through an automated image segmentation, and the new polar images are formed based on linear interpolation so that each side of the image is aligned with the wire in the polar image through the processes described in below. This ensures each image contains complete information in one rotation cycle. In other words, the wire artifact acts as an image-based triggering signal for each B-scan. First, the polar images are stitched together horizontally based on the processing window size to create one continuous image [**Fig. 3(a)**]. Then, the location of the wire for the micromotor is identified using image thresholding [**Fig. 3(b)**]. The wire creates higher reflection compared to the sheath and image artifacts. The thresholding value was empirically set to minimize the noise while capturing as much wire signal as possible. The remaining noise in the resulting binary image is then removed using a series of low-level operations to ensure robust NURD correction.

1) Noise reduction: we applied a 3 × 3 median filter to reduce the speckle noise.

2) Morphological operation: Morphological opening operator with a vertical structural element can be applied to separate the desired wire signal from glass capillary and sheath

Biomedical Optics EXPRESS

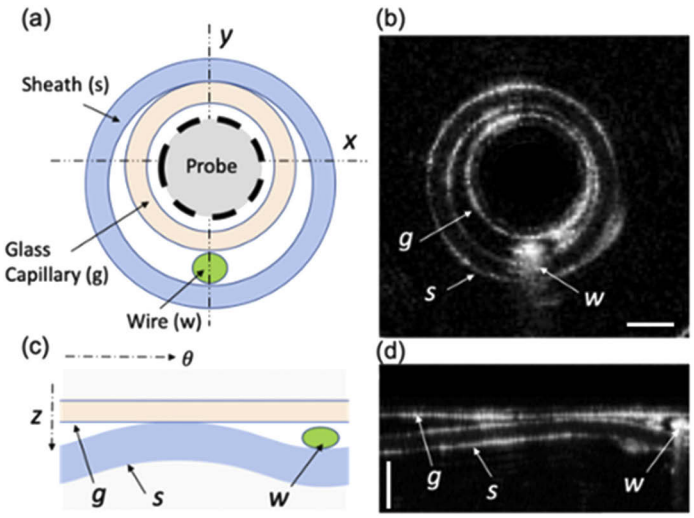

Fig. 2. Center portion of the OCT image that contains the catheter sheath and the metal wire. (a,c) Schematics represented in Cartesian and polar coordinates. (b, d) OCT images represented in Cartesian and polar coordinates. g: glass capillary tube; s: sheath; w: wire. Scale bar: 0.5 mm.

signals. The wire signal appears to be vertically elongated due to the tail artifact, while the glass capillary and sheath appear as thin lines. In our case, we empirically set the size of structural element as 20×70 pixels, which effectively extracted only the wire signals [**Fig. 3(c)**].

3) Area filtering: once the thresholding and morphological opening is applied, any connected regions smaller than a certain pixel (e.g., 200 pixels) are removed to reduce the noise.

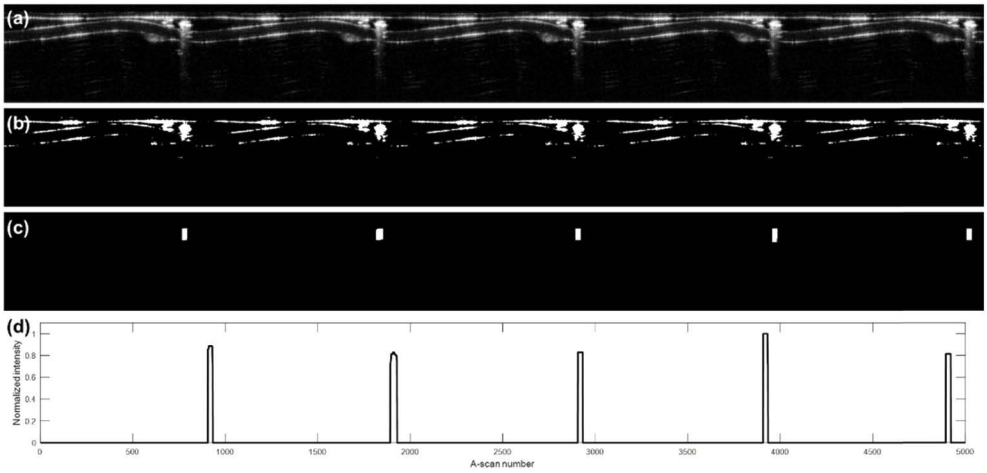

Fig. 3. Image-based trigger generation in the proposed NURD correction algorithm. (a) Stitched OCT image of the sheath portion after (b) binarization, (c) morphological operation. (d) The mean A-line intensity of the binarized image.

Once the binary images of the metal wire are created, the centroid of each wire is identified using a peak detection algorithm [**Fig. 3(d)**]. Here, the minimum and maximum pixel interval

Biomedical Optics EXPRESS

between the two wires were set to guide the peak detection. This first step applies a linear transformation to the image; however, NURD can also cause localized nonlinear deformation within a single B-frame, which needs to be further corrected.

In the second step of the NURD correction algorithm, undersampled or oversampled regions within the image are identified based on dynamic programming (DP) segmentation of the sheath surface profile [26]. Then, a non-linear transformation is applied to correct the local distortion. This step takes advantage of the off-center positioning of the probe with respect to the outer sheath. As the sheath surface profile in the polar image will follow a non-linear profile, the location of the sheath surface can be segmented and used to correct local image distortion. In this study, we defined a normalized cumulative function S_i of i-th angular position as below:

$$S_i(\theta) = \ norm\left[\sum_{i=1}^{\theta}(z_i(\theta) + \tau)\right] \tag{1}$$

where $z(\theta)$ is the height position of the sheath surface at i-th angular position and τ is an arbitrary offset. In **Fig. 4**, we describe two cases of image distortion. In the case described in the red line, the motor rotates faster at first and then slower at the end. This will distort the image and the S(θ) function towards the left side. In the other case described in the blue line, the motor rotates slower at the beginning and faster at the end. This will distort the image and the S(θ) function towards the right side. To correct the nonlinearity, the obtained plot is resampled to match the reference curve using linear interpolation. The reference curve is obtained by averaging all the 200 OCT images and segmenting the sheath profile of the mean image. Offset is varied experimentally to adjust the amount of correction to apply. If the offset is too small, the algorithm will fail to scale the edge as the slope of the function will be close to zero. If the offset is too large, the algorithm will make less correction to the image since the cumulative plot will approach a linear function. In this study, we applied a fixed offset value to all the B-scan frames. While setting adaptive offset for every B-frame can potentially improve the correction accuracy, this requires assessing and setting offset value based on the NURD severity of each image, which will add additional complexity to the processing.

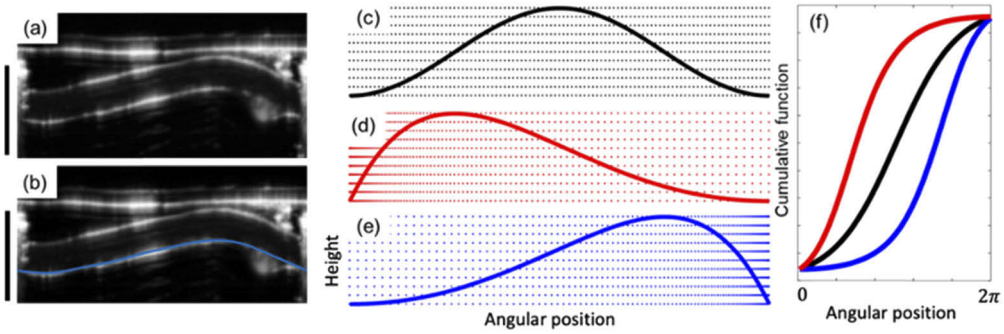

Fig. 4. Characterization and correction of distortion through the nonlinear surface profiled of the sheath. (a) Polar OCT image of sheath location, (b) segmentation of the sheath surface, (c) sheath surface profile without image distortion, (d,e) sheath profiled under NURD distortion, (f) cumulative function of the sheath profile without image distortion (black) and with image distortion (red and blue). Scale bar: 0.5 mm.

2.4. *Evaluating the performance of the correction*

To evaluate the effect of the NURD correction, we performed quantitative analysis on the M-B mode of the dynamic airway images. The M-B mode was created by resampling the 3D data set

Biomedical Optics EXPRESS

of polar OCT images so that the x-axis was the scanning angle and the y-axis was time in each image. Then, intensity projection was performed in the depth direction to obtain the summation of the pixel intensity. The M-B mode contained distinct edges created by the shadow cast on the tissue. Motion artifacts and NURD made the edge features discontinuous and deviate from a straight line. To obtain a quantitative assessment of the amount of image distortion, the deviation in the edge in time was visualized.

In addition, we quantitatively assess the amount of motion in the B-scans using intensity variance projection of 20 consecutive images. For this study, we selected airway images during the resting state when there is little tissue movement. Hence, high intensity variance indicates the mismatch between the frames due to the image distortion or the motion artifacts. Here, the difference index is defined as follows:

$$D(\theta) = \frac{1}{M-1}\sum_{z=1}^{M}\left[\frac{1}{N-1}\sum_{i=1}^{N}\left(I_i(z,\theta) - \overline{I(z,\theta)}\right)^2\right] \tag{2}$$

where M is the number of pixels in A-scan, N is the total number of B-scans, $I_i(z,\theta)$ is the pixel intensity at i-th frame, and $\bar{I}$ is the mean pixel intensity. The mean of the difference index at each A-line was evaluated at each step of the NURD correction.

2.5. Localized compliance measurement

Dynamic OCT images contain information on temporally varying tissue deformation during a respiratory cycle. In this study, the variance of the tissue displacement at each angle position in the polar OCT image was calculated as localized airway compliance. A dynamic programming segmentation algorithm was used to identify the lumen-air boundary in each image and to track the tissue displacement movement. Here, to simplify the localized compliance estimation, we assumed the gross movement of the probe is minimum during the dynamic airway measurement. The final LC value is defined as below:

$$LC(\theta) = \frac{\left[\sum_{n=1}^{N}\left(u(n,\theta) - \overline{u(\theta)}\right)^2\right]}{(P_{max} - P_{min}) \times N} \tag{3}$$

where N is the total number of B-scans, $u(n,\theta)$ is the distance of the tissue surface from the imaging probe at i-th angular position and n-th B-scan, and $\overline{u(\theta)}$ indicates the mean of u at each angular position. In this study, we estimated the LC value from 200 B-scan images. P_{max} and P_{min} are the maximum and minimum intranasal pressure recorded from the pressure transducer.

3. Results and discussion

In a micromotor-based imaging probe, the main cause of NURD is the instability in the motor rotation due to an imbalance in the motor weight, disturbance in the driving voltage, or mechanical resistance in the rotational path [27]. As a result, the acquired image will be either under-sampled or over-sampled. In the compliance measurement, NURD will make the tracking of local tissue displacement difficult as it creates translation and nonlinear deformation of the image. One effective technique for NURD correction is image registration based on structural landmarks such as the wire artifact or fiducial marker [25,28]. However, a wire can cast shadows to the tissue of interest in the OCT images and limit the field of view. In addition, identification of the exact location of the under-sampled or over-sampled region is still challenging, and improper correction can distort the image further. Other methods rely on correlating the speckle contrast in adjacent A-scans to determine the rotation speed [23,24,29]. However, the region with weak image contrast will lead to incorrect NURD correction. In fact, OCT light was partially blocked by nasal hair in the OCT images we acquired, casting shadows in the upper airway tissue. Finally,

Biomedical Optics EXPRESS

Sun *et al.* proposed a method based on the phase shift of the acquired spectral interferogram induced by the NURD in the sheath signal to correct distortion [30]. Although this distortion correction method does not rely on the tissue contrast, high phase stability of the interferometer is required, adding additional complexity and restriction to the imaging system.

To evaluate the feasibility and robustness of the proposed 2-step NURD correction algorithm, we obtained the M-B mode projection view of 200 dynamic OCT images during a respiratory cycle (**Fig. 5**). In the M-B mode projection, we found the edges near the adenoid portion can be easily distinguished due to the shadows cast by the metal wire and the nasal hair (**Fig. 5(a)**). Therefore, we used this section of the image for evaluating the NURD correction as shown in **Fig. 5(b)**. As expected, NURD distorts the polar images and shifts the lateral position of the tissue in the image as indicated by the red arrows in **Fig. 5(c)**. After the alignment process, the lateral motion is reduced (**Fig. 5(d)**). However, the first correction does not improve, if not worsen, the distortion in the center of the image (the example of worsened part is described in the next paragraph). This confirms the necessity to apply the second NURD correction. After applying the nonlinear scaling based on the graph cut theory, the variance in the images was minimized in both the center and the edge (**Fig. 5(e)**).

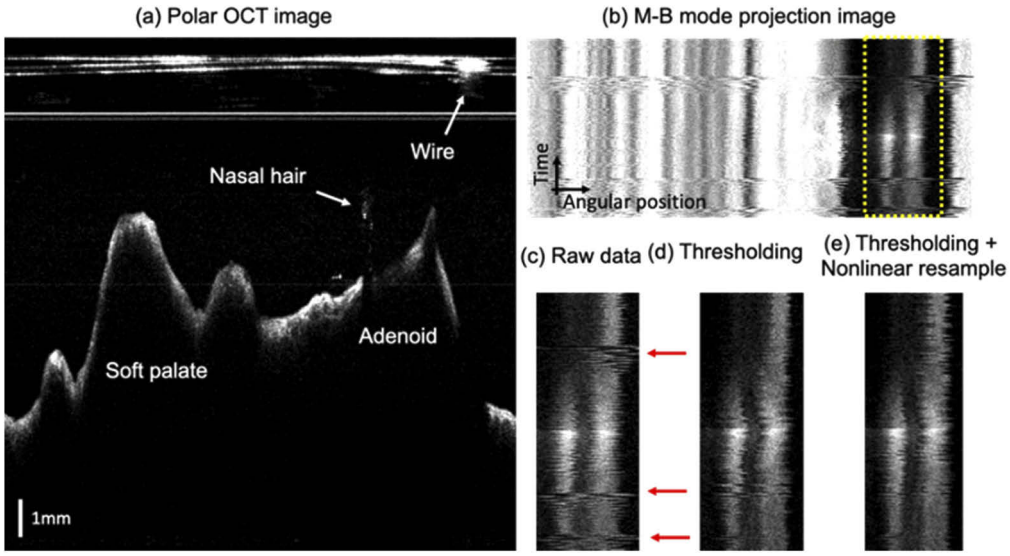

Fig. 5. NURD correction on the dynamic OCT images. (a) Polar OCT images, (b) M-B mode projection of the 200 dynamic OCT B-scan, (c) zoom in view of the yellow box in M-B mode, (d) after applying thresholding to align the image, and (e) after applying thresholding and nonlinear resampling.

Next, we evaluated the accuracy using the intensity variance projection of 20 consecutive B-scan images. The raw OCT data set before the NURD correction shows broadening in the edge features as well as the ghost image formed by the image distortion as indicated by the white arrow in **Fig. 6(a)**. After applying the thresholding method and realignment of the images, the ghost image in the adenoid in the original image has improved. However, the image distortion of the center part of the image has become worse as indicated by the broadening in the edge features near the center region [**Fig. 6(b)**]. After realignment and nonlinear resampling, the image distortions are significantly reduced in both the center and peripheral part of the image [**Fig. 6(c)**]. The improvement in the image distortion can also be confirmed from the decrease in the difference index where $D_{raw} = 75 \pm 129$, $D_{threshold} = 58 \pm 74$, $D_{resample} = 44 \pm 57$ [**Fig. 6(d)**]. We also confirmed the improvement in the NURD using the assessment index based on the

Biomedical Optics EXPRESS

geographic area of the lumen across B-scan images. The lumen was segmented using the dynamic programming segmentation algorithm from the polar OCT image and the pixels inside the lumen were counted as cross-sectional area (CSA). After applying the 2-step NURD correction algorithm, the CSA curve showed less fluctuation and smooth changes in the geographic area across time, indicating less image distortion (Supplement 1).

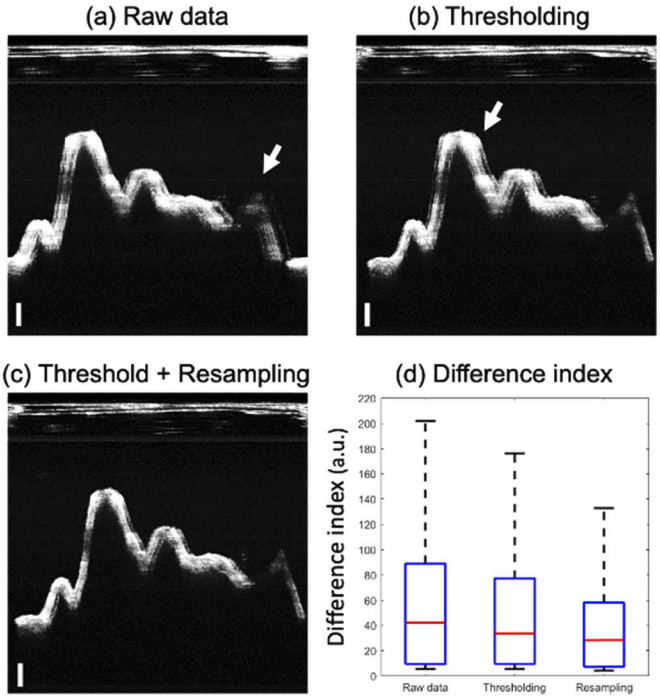

Fig. 6. Projection view of pixel intensity variance across B-scan. (a) Raw data and after applying (b) thresholding and (c) nonlinear resampling. White arrows show the regions of image distortion. (d) Box plot of difference index. Scale bar: 1 mm.

Dynamic OCT imaging of a human nasopharynx was obtained during the inspiration of a respiratory cycle (see **Visualization 1**). During inhalation, negative pressure will be generated in the airway and partially collapse the lumen. Since the anterior segment that contains soft pallet consists of low elasticity material, there is little movement in response to the pressure changes. On the other hand, the posterior segment that contains adenoid in the nasopharynx consists of soft tissue and, thus, shows larger displacement. The adenoid is a mass of lymphatic tissue in the roof of the nasopharynx, playing a role in the immune system. It is known that infection or hypertrophy in the adenoid tissue can obstruct the flow of air. In our localized compliance measurement, the posterior region had much higher compliance value compare to the surrounding area, indicating the part near the adenoid being susceptible to airway collapse. On the other hand, the lateral walls of the nasopharynx are made of the pharyngeal ostia of the auditory tube and supported by cartilage tissue, providing relatively low tissue compliance. In the acquired OCT image, there are two fold structures arising from the cartilaginous opening of the auditory tube in the lateral portion. In this study, we estimated the localized compliance of the tissue based on the changes in the distance from the imaging probe. However, the gross motion of the probe position can cause error in this type of localized compliance estimation, which can be compensated by estimating the geometrical center of the lumen. [22]

Biomedical Optics EXPRESS

Tissue surface was segmented using the same graph cut algorithm and plotted during inspiration. The 3D spatiotemporal map of the tissue surface shows the displacement in the tissue height from 800 to 1000 A-line location indicated by the arrow in **Fig. 7(a)**. This location corresponds to the adenoid. The LC index is calculated at each A-line location by taking the variance of the axial displacement [**Fig. 7(b)**]. As expected, the adenoid had high compliance compared to the surrounding tissue.

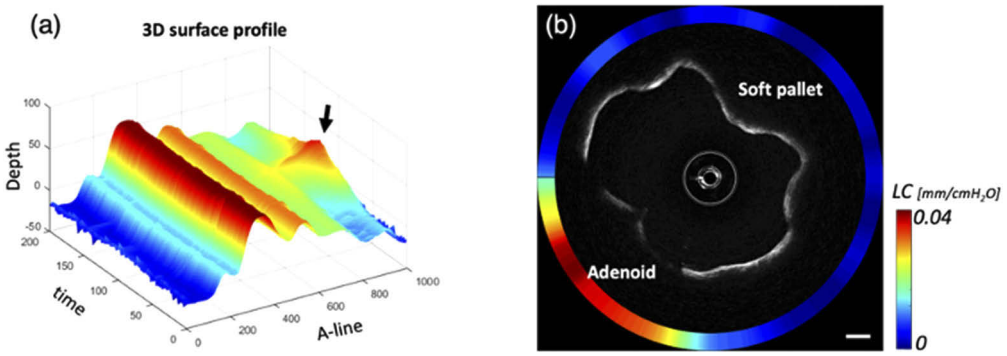

Fig. 7. Localized compliance measurement. (a) Time-varying displacement map of the nasopharynx and the location corresponds to the adenoid indicated by black arrow. (b) Localized airway compliance index at each angle position displayed in Cartesian coordinate. Scale bar: 2 mm.

For clinical application and the compliance measurement of human subjects, the protective sheath can be replaced after each imaging session to avoid contamination as well as the sheath wear and tear. Besides keeping the sheath sterile, it is important to maintain the sheath surface clean and free of damage in order to acquire good imaging quality. In addition, due to the complex anatomical structure of the upper airway, the imaging catheter can occasionally experience excessive stress and be bent. While the bending of the catheter does not generally increase the amount of NURD in the micromotor-based imaging, the excessive bending angle can potentially damage the metal wire or the optical fiber.

4. Summary and conclusion

We presented a new NURD correction technique that allows the correction of image distortion in a micromotor imaging probe. Imaging thresholding is first applied to the wire signal to align the image and then graph-based segmentation of the nonlinear surface profile of the catheter sheath is used to correct the imaging distortion. This technique does not rely on tissue contrast and only uses the information from the motor wire and the catheter sheath. The M-B mode projection view demonstrates the effectiveness of the proposed NURD correction technique. Furthermore, we constructed a LC map based on the corrected images in the human nasopharynx. To the best of our knowledge, this is the first OCT study to characterize in vivo localized compliance measurement of the adenoid in an awake human.

Funding. National Institute of Environmental Health Sciences (U54 ES027698); Air Force Office of Scientific Research (FA9550-20-1-0052); National Institutes of Health (R01EB-030024, R01EY-026091, R01HL-125084, R01HL-127271).

Acknowledgments. We thank the individual who participated in the human study.

Disclosures. The authors declare no conflicts of interest.

Data availability. The data that support the findings of this study are available on request from the corresponding author, Z.C.

Supplemental document. See Supplement 1 for supporting content.

Biomedical Optics EXPRESS

References

1. A. Sarvazyan, T. J. Hall, M. W. Urban, M. Fatemi, S. R. Aglyamov, and B. S. Garra, "An overview of elasticity imaging - an emerging branch of medical imaging," Curr. Med. Imaging Rev. **7**(4), 255–282 (2011).
2. P. Kennedy, M. Wagner, L. Castéra, C. W. Hong, C. L. Johnson, C. B. Sirlin, and B. Taouli, "Quantitative elastography methods in liver disease: current evidence and future directions," Radiology **286**(3), 738–763 (2018).
3. E. Yılmaz, A. Yılmaz, A. Aslan, I. Inan, M. C. Evren, and K. Tekesin, "Real-time elastography for differentiation of breast lesions," pjr **82**, 664–669 (2017).
4. K. P. Strohl, J. P. Butler, and A. Malhotra, "Mechanical properties of the upper airway," Compr. Physiol. **2**(3), 1853–1872 (2012).
5. O. F. Pedersen and T. M. Nielsen, "The compliance curve for the flow limiting segments of the airway: II. Experiments with human subjects," Acta Physiol. Scand. **100**(2), 139–153 (1977).
6. C. Robertson, S.-W. Lee, Y.-C. Ahn, S. Mahon, Z. Chen, M. Brenner, and S. C. George, "Investigating in vivo airway wall mechanics during tidal breathing with optical coherence tomography," J. Biomed. Opt. **16**(10), 106011 (2011).
7. M. Marques, P. R. Genta, A. Azarbarzin, S. A. Sands, L. Taranto-Montemurro, L. Messineo, D. P. White, and A. Wellman, "Retropalatal and retroglossal airway compliance in patients with obstructive sleep apnea," Respir. Physiol. Neurobiol. **258**, 98–103 (2018).
8. P. R. Genta, B. A. Edwards, S. A. Sands, R. L. Owens, J. P. Butler, S. H. Loring, D. P. White, and A. Wellman, "Tube law of the pharyngeal airway in sleeping patients with obstructive sleep apnea," Sleep **39**(2), 337–343 (2016).
9. S. D. Murgu and H. G. Colt, "Tracheobronchomalacia and excessive dynamic airway collapse," Respirology **11**(4), 388–406 (2006).
10. B. C. Harvey, K. R. Lutchen, and P. E. Barbone, "Spatial distribution of airway wall displacements during breathing and bronchoconstriction measured by ultrasound elastography using finite element image registration," Ultrasonics **75**, 174–184 (2017).
11. C. H. Chang, C. C. Huang, Y. H. Wang, F. J. Chou, and J. W. Chen, "Ultrasound shear-wave elastography of the tongue in adults with obstructive sleep apnea," Ultrasound Med. Biol. **46**(7), 1658–1669 (2020).
12. B. Jiang, X. L. Li, Y. Yin, Q. Zhang, T. Zang, W. S. Song, X. M. Wang, J. Kang, F. J. F. Herth, and G. Hou, "Ultrasound elastography: A novel tool for the differential diagnosis of pleural effusion," Eur Respir J **54**(2), 1802018 (2019).
13. S. Cheng, S. C. Gandevia, M. Green, R. Sinkus, and L. E. Bilston, "Viscoelastic properties of the tongue and soft palate using MR elastography," J. Biomech. **44**(3), 450–454 (2011).
14. F. Fakhouri, H. Dong, and A. Kolipaka, "Magnetic resonance elastography of the lungs: a repeatability and reproducibility study," NMR Biomed. **32**(7), e4102 (2019).
15. J. Jing, J. Zhang, A. C. Loy, B. J. F. Wong, and Z. Chen, "High-speed upper-airway imaging using full-range optical coherence tomography," J. Biomed. Opt. **17**(11), 110507 (2012).
16. G. K. Sharma, G. S. Ahuja, M. Wiedmann, K. E. Osann, E. Su, A. E. Heidari, J. C. Jing, Y. Qu, F. Lazarow, A. Wang, L. Chou, C. C. Uy, V. Dhar, J. P. Cleary, N. Pham, K. Huoh, Z. Chen, and B. J.-F. Wong, "Long-range optical coherence tomography of the neonatal upper airway for early diagnosis of intubation-related subglottic injury," Am. J. Respir. Crit. Care Med. **192**(12), 1504–1513 (2015).
17. J. C. Jing, L. Chou, E. Su, B. J. F. Wong, and Z. Chen, "Anatomically correct visualization of the human upper airway using a high-speed long range optical coherence tomography system with an integrated positioning sensor," Sci. Rep. **6**(1), 39443 (2016).
18. S. L. Davidson, R. Amin, R. Arens, Z. Chen, S. Davis, E. Gutmark, R. Superfine, B. Wong, C. Zdanski, and M. C. K. Khoo, "Pediatric sleep-related breathing disorders: advances in imaging and computational modeling HHS Public Access," IEEE Pulse **5**(5), 33–39 (2014).
19. M. S. Leigh, J. J. Armstrong, A. Paduch, J. H. Walsh, D. R. Hillman, P. R. Eastwood, and D. D. Sampson, "Anatomical optical coherence tomography for long-term, portable, quantitative endoscopy," IEEE Trans. Biomed. Eng. **55**(4), 1438–1446 (2008).
20. J. P. Williamson, R. A. McLaughlin, W. J. Noffsinger, A. L. James, V. A. Baker, A. Curatolo, J. J. Armstrong, A. Regli, K. L. Shepherd, G. B. Marks, D. D. Sampson, D. R. Hillman, and P. R. Eastwood, "Elastic properties of the central airways in obstructive lung diseases measured using anatomical optical coherence tomography," Am. J. Respir. Crit. Care Med. **183**(5), 612–619 (2011).
21. R. Bu, S. Balakrishnan, N. Iftimia, H. Price, C. Zdanski, and A. L. Oldenburg, "Airway compliance measured by anatomic optical coherence tomography," Biomed. Opt. Express **8**(4), 2195–2209 (2017).
22. R. Bu, S. Balakrishnan, H. Price, C. Zdanski, S. Mitran, and A. L. Oldenburg, "Localized compliance measurement of the airway wall using anatomic optical coherence elastography," Opt. Express **27**(12), 16751 (2019).
23. G. van Soest, J. G. Bosch, and A. F. W. van der Steen, "Azimuthal registration of image sequences affected by nonuniform rotation distortion," IEEE Trans. Inform. Technol. Biomed. **12**(3), 348–355 (2008).
24. E. Abouei, A. M. D. Lee, H. Pahlevaninezhad, G. Hohert, M. Cua, P. Lane, S. Lam, and C. MacAulay, "Correction of motion artifacts in endoscopic optical coherence tomography and autofluorescence images based on azimuthal en face image registration," J. Biomed. Opt. **23**(01), 1–13 (2018).
25. O. O. Ahsen, H.-C. Lee, M. G. Giacomelli, Z. Wang, K. Liang, T.-H. Tsai, B. Potsaid, H. Mashimo, and J. G. Fujimoto, "Correction of rotational distortion for catheter-based en face OCT and OCT angiography," Opt. Lett. **39**(20), 5973 (2014).

Biomedical Optics EXPRESS

26. L. Qi, S. Huang, A. E. Heidari, C. Dai, J. Zhu, and Z. Chen, "Automatic airway wall segmentation and thickness measurement for long-range optical coherence tomography images," Opt. Express **23**(26), 33992 (2015).
27. J. Mavadia-Shukla, J. Zhang, K. Li, and X. Li, "Stick-slip nonuniform rotation distortion correction in distal scanning optical coherence tomography catheters," J. Innov. Opt. Health Sci. **13**(06), 2050030 (2020).
28. G. J. Ughi, "Automatic three-dimensional registration of intravascular optical coherence tomography images," J. Biomed. Opt. **17**(2), 026005 (2012).
29. N. Uribe-Patarroyo and B. E. Bouma, "Rotational distortion correction in endoscopic optical coherence tomography based on speckle decorrelation," Opt. Lett. **40**(23), 5518 (2015).
30. C. Sun, F. Nolte, K. H. Y. Cheng, B. Vuong, K. K. C. Lee, B. A. Standish, B. Courtney, T. R. Marotta, A. Mariampillai, and V. X. D. Yang, "In vivo feasibility of endovascular Doppler optical coherence tomography," Biomed. Opt. Express **3**(10), 2600 (2012).